Original Paper

Synthesis of hierarchical SAPO-11-based catalysts with Al-based metal-organic framework derivative as mesoporogen to improve n-decane branched isomerization

Xue-Man Wang [a], Cheng-Long Wen [b, **], Yu Fan [a, *]

[a] State Key Laboratory of Heavy Oil Processing, China University of Petroleum, Beijing, 102249, China
[b] Jiangsu Key Laboratory of Advanced Catalytic Materials and Technology, Advanced Catalysis and Green Manufacturing Collaborative Innovation Center, and School of Petrochemical Engineering, Changzhou University, Changzhou, Jiangsu, 213164, China

A R T I C L E   I N F O

A B S T R A C T

Hierarchical SAPO-11 molecular sieve (ACS-11) was successfully synthesized employing the Al_2O_3/carbon (Al_2O_3/C) composite obtained through the pyrolysis of Al-based metal-organic framework (Al-MOF-96) as mesoporogen. Unlike other carbon-based mesoporogens with strong hydrophobicity, the Al_2O_3/C interacts with phosphoric acid and generates the $AlPO_4$/C structure, which promotes the Al_2O_3/C dispersion in the synthesis gel of SAPO-11 and avoids the phase separation between them. The Al_2O_3/C as mesoporogen decreases the crystallite size of SAPO-11 via preventing the aggregation of SAPO-11 crystals. Additionally, the addition of Al_2O_3/C improves the Si distribution in the ACS-11 framework. Consequently, ACS-11 has smaller crystallites, more mesopores, and a greater amount of medium Brønsted acid centers than the conventional microporous SAPO-11 and the SAPO-11 synthesized using activated carbon as mesoporogen. The corresponding Pt/ACS-11 catalyst exhibits the maximal selectivity to multi-branched C_{10} isomers (23.28%) and the minimal cracking selectivity (15.83%) in n-decane hydroisomerization among these catalysts. This research provides a new approach for preparing hierarchical silicoaluminophosphate molecular sieve-based catalysts to produce high-quality fuels.
© 2022 The Authors. Publishing services by Elsevier B.V. on behalf of KeAi Communications Co. Ltd. This is an open access article under the CC BY-NC-ND license (http://creativecommons.org/licenses/by-nc-nd/4.0/).

1. Introduction

With the growing attachment to the environmental issues, the production of clean gasoline has become a major assignment in petroleum refining industry. To this end, the strict gasoline quality standards have been formulated by countries all over the world, limiting the contents of olefins and aromatics in gasoline. The decrease in the contents of high-octane olefins and aromatics will unavoidably cause the great reduction of gasoline octane number. n-alkane hydroisomerization is a process that converts low-octane straight chain paraffin into their high-octane branched alkanes (Qin et al., 2011; Samad et al., 2016; Kim et al., 2018; Jaroszewska et al., 2019). In this process, bifunctional catalysts containing metal sites and acid sites are often adopted in alkane hydroisomerization, and

the metal sites provide the (de)hydrogenation active sites and acid sites provide skeletal isomerization active sites (Kim et al., 2013; Liu et al., 2015; Yu et al., 2020). In general, the metal sites are usually supplied by precious metals (such as platinum and palladium) (Lv et al., 2018; Oenema et al., 2020.), non-precious metals (such as nickel and MoO_x) (Yang et al., 2019; Harmel et al., 2020) and bimetallic nanoparticles (such as Pt—Ni and Pt—Ni_2P) (Eswaramoorthi and Lingappan, 2003; Yao et al., 2015), and the acid sites are normally offered by silica-alumina zeolites (such as ZSM-22, Beta, ZSM-5 and Y) (Chi et al., 2013; Jin et al., 2009; Lee et al., 2013; Sazama et al., 2018), silicoaluminophosphate (SAPO-n) (Zhao et al., 2020; Guo et al., 2021; Wen et al., 2021), metal oxides (such as SO_4^{2-}/ZrO_2) (Kimura, 2003) and mesoporous materials (such as AlSBA-15 and Al-TUD-1) (Kang et al., 2021; Vedachalam et al., 2021). Among them, Pt has an excellent hydrogenation/dehydrogenation activity, and SAPO-11 possesses mild acidity and an appropriate pore structure for different processes (Sánchez-Contador et al., 2018). Hence, the Pt/SAPO-11 catalysts are extensively used on alkane hydroisomerization (Zhang et al., 2018a).

* Corresponding author.
** Corresponding author.
    E-mail addresses: wenchenglong@cczu.edu.cn (C.-L. Wen), fanyu@cup.edu.cn (Y. Fan).

However, mono-branched (Mo) isomers instead of multi-branched (Mu) isomers are the principal products for alkane hydro-isomerization over Pt/SAPO-11 due to the small micropore size (0.39×0.63 nm) and external surface area (ESA) of conventional SAPO-11. The Mu isomers with higher octane numbers than the Mo isomers are optimal components to improve gasoline octane number (Liu et al., 2014). Researches show that the hierarchical SAPO-11 is able to effectively improve the selectivity to Mu isomers (Nandan et al., 2014; Zhao et al., 2019). Thus, it is of great significance to synthesize SAPO-11 molecular sieve with a hierarchical structure.

There are many methods to synthesize hierarchical molecular sieves, such as desilication or dealumination, hard template strategy and soft template strategy (Jacobsen et al., 2000; Fan et al., 2012; Xi et al., 2014; Chen et al., 2016). However, in desilication or dealumination, the amount of removed silicon or aluminum cannot be controlled, and the excessive removal of framework silicon or aluminum will affect the crystallinity and stability of molecular sieves (Cartlidge et al., 1989; Groen et al., 2004). The soft template strategy is limited because the soft templates have a competition with the micropore templates to degrade the crystallization of molecular sieves and cause more environmental pollution in the process of removing soft templates. For the synthesis of hierarchical molecular sieves with a hard template strategy, the process is usually simple and the hard templates used do not interfere with the micropore templates. Thereby, the synthesis of hierarchical molecular sieves using hard templates has aroused extensive attention. Carbon materials, as a kind of hard templates, are commonly applied in the synthesis of hierarchical molecular sieves (Jacobsen et al., 2000; Christensen et al., 2005). However, the phase separation, which exists between carbon materials and synthesis precursor gel of hierarchical molecular sieves, is easy to occur, and which is attributed to the weak hydrophilicity of carbon materials (Machoke et al., 2015). To improve the hydrophilicity of carbon materials, Zhao et al. (2019) prepared carbon nanoparticles with abundant -C-O-C- groups by calcining a mixture of urea and polyethylene oxide in N_2, and the -C-O-C- groups were converted into the -C-O-H groups in the alkali synthetic solution of hierarchical ZSM-5 molecular sieve. The existence of -C-O-H groups enhances the interaction between the carbon nanoparticles and ZSM-5 synthesis gel, and thus the hierarchical ZSM-5 with large mesopore size was successfully obtained. Bértolo et al. (2014) adopted a new process to obtain the hierarchical SAPO-11 through the use of commercial Merck carbon and Merck carbon with the treatment of nitric acid as mesoporogen, respectively. Merck carbon treated with nitric acid has more amount of oxygenate surface groups compared to the commercial Merck carbon, but the ESA and mesopore volume of the hierarchical SAPO-11 using Merck carbon with the treatment of nitric acid as the template are almost the same as those of the hierarchical SAPO-11 obtained by employing Merck carbon as mesoporogen.

Metal-organic frameworks (MOFs) have aroused considerable attention because of their diversity of pore structures and high specific surface areas (Yang et al., 2022; Zhang et al., 2022) over recent years. The composites with the uniform mixture of carbon and metal oxides can be prepared through the heat treatment of MOFs (Li et al., 2022; Liu et al., 2022). Al-MOF-96, a typical porous aluminum based metal organic framework material, has the characteristics of simple synthesis and large-scale production (Deng and Peng, 2019), which can be used to prepare the composites with the uniform mixture of carbon and Al_2O_3. Additionally, Al_2O_3 can interact with phosphoric acid, thereby forming the aluminophosphate layers (Zhang et al., 2018b). Thus, compared with conventional carbon materials, the Al_2O_3/C composite has better hydrophilicity in the phosphoric acid solution. However, the hierarchical molecular sieves prepared by using the metal oxide/carbon composite derived from MOFs as the mesoporogen has not been reported.

In this work, a novel Al_2O_3/C composite derived from Al-MOF-96 was used to synthesize hierarchical SAPO-11. The above synthesized hierarchical SAPO-11 has more mesopores, a greater ESA and a higher number of medium Brønsted acid centers (MBAC) than the conventional SAPO-11 (S-11) and the hierarchical SAPO-11 obtained employing activated carbon as the mesoporogen (CS-11). As a result, its corresponding catalyst displays enhanced selectivity to branched C_{10} isomers and low cracking selectivity in the n-decane hydroisomerization.

2. Experimental

2.1. Materials

Pseudoboehmite (73.0 wt% PB) was purchased from Shandong Aluminum Plant. Tetraethoxysilane (99.0 wt% TEOS), trimesic acid (98 wt% $C_6H_3(CO_2H)_3$), di-n-propylamine (99.5 wt% DPA), phosphoric acid (85.0 wt% H_3PO_4) and activated carbon (AR 200 mesh) were purchased from Aladdin. n-decane (98 wt% $C_{10}H_{22}$), aluminum nitrate (99 wt% $Al(NO_3)_3 \cdot 9H_2O$) and chloroplatinic acid (37.0 wt% $H_2PtCl_6 \cdot 6H_2O$) were provided by Innochem. Deionized water (H_2O) was made in the laboratory. All reagents were employed directly as purchased.

2.2. Synthesis of SAPO-11

2.2.1. Synthesis of conventional S-11

The synthesis procedures of conventional SAPO-11 were consistent with literature (Wen et al., 2021), which is shown as detailed below: firstly, 12.2 g of H_3PO_4 and 40.0 g of H_2O were mixed thoroughly, followed by adding 8.1 g of PB and evenly stirring for 3 h. Subsequently, 4.7 g of TEOS and 6.8 g of DPA were added to the suspension in turn and stirred for 3 h to afford the mixture with the composition of 40 H_2O: 0.95 P_2O_5: 1.2 DPA: 0.4 TEOS: 1.0 Al_2O_3. Finally, the above synthesis mixture was poured into a 100 mL autoclave to crystallize at 200 °C for 24 h. The resultant sample was obtained after washing, drying and calcination at 600 °C for 6 h for the removal of DPA, and it was denoted as S-11.

2.2.2. Synthesis of ACS-11

The preparation procedures of hierarchical SAPO-11 with $Al_2O_3/$C as mesoporogen were as follows. First, Al-MOF-96 was synthesized through the method described in literature (Liu et al., 2015), and then the Al_2O_3/C composite was obtained after the calcination of Al-MOF-96 at 600 °C for 2 h in N_2. Subsequently, 1.5 g of Al_2O_3/C composite was added to the mixture with the composition of 12.2 g of H_3PO_4 and 40.0 g of H_2O and mixed thoroughly for 4 h. Afterwards, 7.0 g of PB and 4.7 g of TEOS were added in turn and evenly mixed for 5 h. Whereafter, 6.8 g of DPA was dropwise added to the solution and mixed for 1 h. Finally, the resulting mixture was put into a 100 mL autoclave and heated at 200 °C for 24 h. The as-synthesized sample was washed, dried and calcined at 600 °C for 6 h to remove DPA and mesoporogen, and it was denoted as ACS-11.

2.2.3. Synthesis of CS-11

The preparation procedures of hierarchical SAPO-11 employing activated carbon as mesoporogen were same as that of ACS-11 except that the activated carbon was utilized as mesoporogen rather than $Al_2O_3/$C. The obtained hierarchical SAPO-11 was named CS-11.

2.2.4. Catalysts preparation

Pt/SAPO-11 catalysts with the platinum mass fraction of 0.5% were obtained via incipient wetness impregnation. First, S-11, CS-11 and ACS-11 were pressed, and then they were sieved to 20−40 mesh. Subsequently, these catalysts were prepared by adding a solution of H_2PtCl_6 to the shaped SAPO-11 samples. Finally, these catalysts were got after drying and calcination at 450 °C for 4 h.

2.3. Characterizations

A D8 Advance X-ray diffractometer (XRD) produced by Bruker AXS was used to analysis the sample structure (a Cu Kα radiation, 40 kV and 40 mA). A scanning electron microscopy (SEM) was performed to analyze the sizes and morphological properties using a SU8010. An ASAP 2420 physical adsorption equipment was adopted to perform the N_2 adsorption-desorption measurement. The micropore volume (V_{micro}) and ESA of the sample were obtained based on the t-plot method (Lippens and Boer, 1965). The specific surface area (S_{BET}) and the pore size distribution of the sample were obtained according to the Brunauer-Emmett-Teller method and the Barrett-Joyner-Halenda method individually (Barrett et al., 1951).

A F20 transmission electron microscopy (TEM) was adopted to obtain the TEM photos and the high-angle annular dark-field scanning transmission electron microscopy (HAADF-STEM) photos of samples. A NICOLE-750 infrared instrument was adopted to measure the acid properties of the samples. The disk sample with 0.02 g was heated at 400 °C for 1 h, then the disk absorbed pyridine vapor for 0.25 h at room temperature. Afterwards, the vacuum desorption of pyridine was carried out at 200 °C and then 300 °C. Eventually, the pyridine infrared (Py-IR) spectrums at 200 and 300 °C were obtained at room temperature. X-ray fluorescence spectroscopy (XRF) was carried out on a ZSX-100e spectrometer to detect the elemental compositions of samples. An Avance III spectrometer with a 4 mm probe head was employed to analyze the Si coordinated environment of the synthesized samples, and the ^{29}Si spectra were recorded at 79.5 MHz and a recycle delay of 3 s. The ^{29}Si shifts are referenced to 3-(trimethylsilyl)-1-propanesulfonic acid sodium salt. H_2 chemical adsorption was carried out to analyze the Pt dispersions of the catalysts by the Auto Chem II 2920 equipment.

2.4. Catalytic tests

n-decane hydroisomerization was performed in a fixed-bed microreactor. First, the catalysts were reduced at 400 °C, 2.0 MPa and a H_2 flow rate of 50 mL/min for 4 h. Afterwards, n-decane hydroisomerization was carried out at 340 °C, 2.0 MPa, a H_2/n-decane volume ratio (HDVR) of 400 and different weight hourly space velocities (WHSVs) of 2.0−25 h^{-1}. The products were qualitatively confirmed using a Trace 1310 mass spectrometry. What is more, the n-decane hydroisomerization products were analyzed adopting an SP3420 gas chromatograph, which contains an HP-PONA column (50 m × 0.25 mm) and an FID detector.

The n-decane conversion, the selectivity to total branched C_{10} isomers (S_T), the selectivity to multi-branched C_{10} isomers (S_{Mu}), the cracking selectivity (S_C), the total branched C_{10} isomers yield (Y_T) and the multi-branched C_{10} isomers yield (Y_{Mu}) were calculated as follows:

$$Conversion = \frac{C_r - C_P}{C_r} \times 100\% \tag{1}$$

$$S_T = \frac{C_T}{C_r - C_P} \times 100\% \tag{2}$$

$$S_{Mu} = \frac{C_{Mu}}{C_r - C_P} \times 100\% \tag{3}$$

$$S_C = \frac{C_C}{C_r - C_P} \times 100\% \tag{4}$$

$$Y_T = \frac{C_T}{C_r} \times 100\% \tag{5}$$

$$Y_{Mu} = \frac{C_{Mu}}{C_r} \times 100\% \tag{6}$$

where C_r represents the concentration of n-decane in the feedstock; C_P and C_T represent the n-decane concentration and total branched C_{10} isomers concentration in the products individually; C_{Mu} represents the multi-branched C_{10} isomers concentrations in products, and C_C is cracking products concentration in products.

n-decane hydroisomerization was considered as a pseudo-first-order reaction (Wen et al., 2017). The rate constant (k) was calculated as detailed below:

$$k = \frac{F}{q} \ln\left(\frac{1}{1-c}\right) \tag{7}$$

where F represents the n-decane feed rate in mol s^{-1}, q and c represent the quality of catalyst (g) and n-decane conversion individually.

The formula adopted to calculate the catalyst turnover frequency (TOF) was as follows (Guo et al., 2013):

$$TOF = \frac{f}{C_B} \tag{8}$$

where f refers to the amount of reacted n-decane per gram of catalyst per second (mol/g/s). C_B represents the numbers of MSBAC in the per catalyst quality (mol/g).

3. Results and discussion

3.1. XRD characterization

Fig. 1 displays the XRD spectra of S-11, CS-11 and ACS-11. All samples appear characteristic peaks at $2\theta = 8.1°$, 9.5°, 13.1°, 15.7°, 20.4°, 21.1° and 22.2−23.3°, which are ascribed to the AEL topology of SAPO-11 (Phienluphon et al., 2015; Wen et al., 2017). The XRD results show that the addition of activated carbon or Al_2O_3/C in the synthesis of SAPO-11 does not change the crystal structure of SAPO-11. Additionally, the XRD patterns of the synthesized SAPO-11 samples appear a weak peak at $2\theta = 6.6°$ attributed to SAPO-41, which is commonly observed in SAPO-11 (Guo et al., 2013; Wen et al., 2021). In the synthesis of SAPO-11, the aluminum phosphate ($AlPO_4$) precursors are first produced, and then Si substitution in the $AlPO_4$ framework occurs. During this process, the slow formation rate of $AlPO_4$ precursors and the fast releasing rate of silicon species lead to a change in the composition of partial liquid phases, which results in the formation of SAPO-41 (Ren et al., 1991; López et al., 1997).
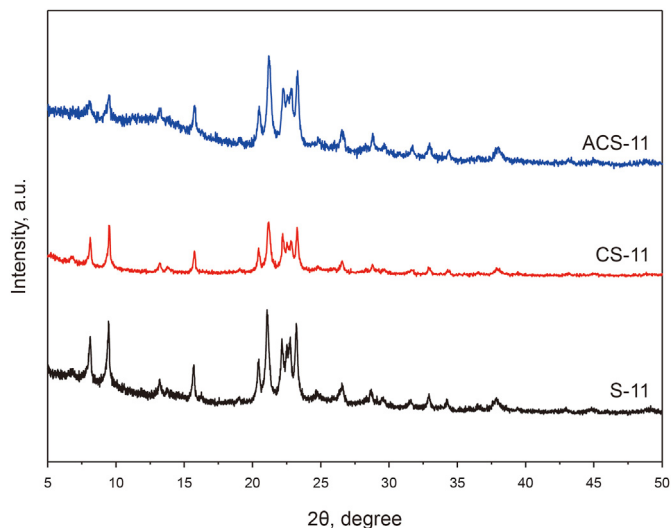
Fig. 1. XRD patterns of S-11, CS-11 and ACS-11.

Fig. 3. Pore diameter distributions of S-11, CS-11 and ACS-11.

3.2. Nitrogen adsorption-desorption characterization

Fig. 2 presents the nitrogen adsorption-desorption isotherms of S-11, CS-11 and ACS-11. CS-11 and ACS-11 exhibit obvious hysteresis loops while S-11 presents a small hysteresis loop in the range of relative pressure $(P/P_0) = 0.4-0.9$, showing that there are more mesopores in CS-11 and ACS-11. According to the SEM results (Fig. S1), the addition of activated carbon or Al_2O_3/C could hinder the aggregation between SAPO-11 crystals, so CS-11 and ACS-11 have more intercrystal mesopores in comparison to S-11.

The pore diameter distributions of S-11, CS-11 and ACS-11 are given in Fig. 3. All samples present a peak at 3.8 nm, which is caused by the tensile strength effect (Danilina et al., 2010). In addition, CS-11 and ACS-11 present high intensity peaks at 6.0 and 6.5 nm, respectively, and S-11 presents a low intensity peak at 5.5 nm, indicating that CS-11 and ACS-11 have abundant mesopores while S-11 has a relatively low amount of mesopores. Additionally, the texture properties of S-11, CS-11 and ACS-11 are exhibited in Table 1. The mesopore volume and ESA of these samples rise in the order S-11 < CS-11 < ACS-11. In addition, as shown in the TEM images (Fig. S2), ACS-11 has much more mesopores than S-11 and CS-11,
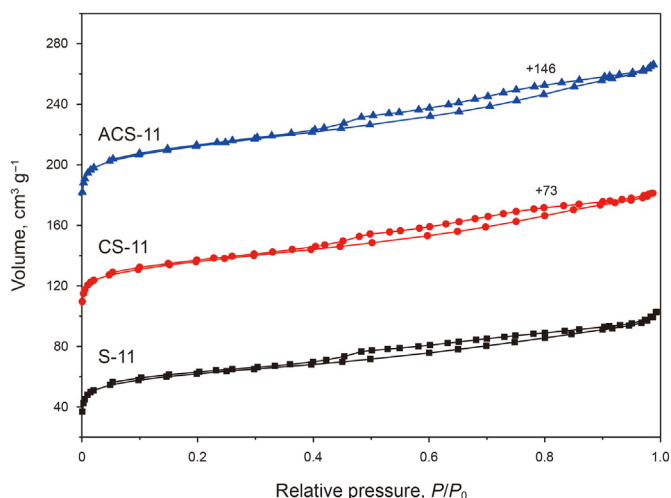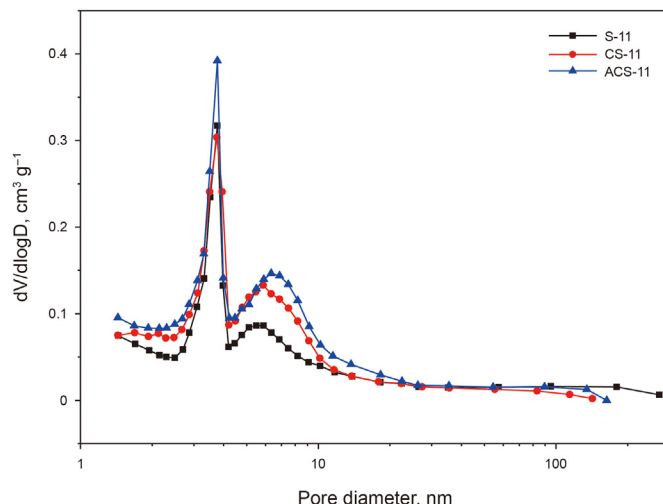
Table 1
Texture properties of S-11, CS-11 and ACS-11.

Sample	S_{BET}, m^2 g^{-1}	$S_{external}$, m^2 g^{-1}	$V_{micropore}$, cm^3 g^{-1}	$V_{mesopore}$, cm^3 g^{-1}
S-11	228	71	0.07	0.08
CS-11	212	91	0.05	0.11
ACS-11	248	108	0.06	0.13

which is in consistence with the nitrogen adsorption-desorption result.

In order to explain the Al_2O_3/C function in the synthesis of hierarchical ACS-11, the Al_2O_3/C composite derived from Al-MOF-96 was treated with phosphoric acid according to the following procedures: Al_2O_3/C (1.5 g) was added to the solution of H_2O (40 g) and phosphoric acid (12.2 g) and stirred for 4 h. Afterwards, the mixture was put into the autoclave and maintained at 200 °C for 24 h. The sample named $H_3PO_4-Al_2O_3/C$ was collected by washing and drying. And the $H_3PO_4-Al_2O_3/C$ and Al_2O_3/C were characterized by XRD.

Fig. 4 displays the XRD spectra of $H_3PO_4-Al_2O_3/C$ and Al_2O_3/C. Al_2O_3/C shows no diffraction peaks, while $H_3PO_4-Al_2O_3/C$ presents
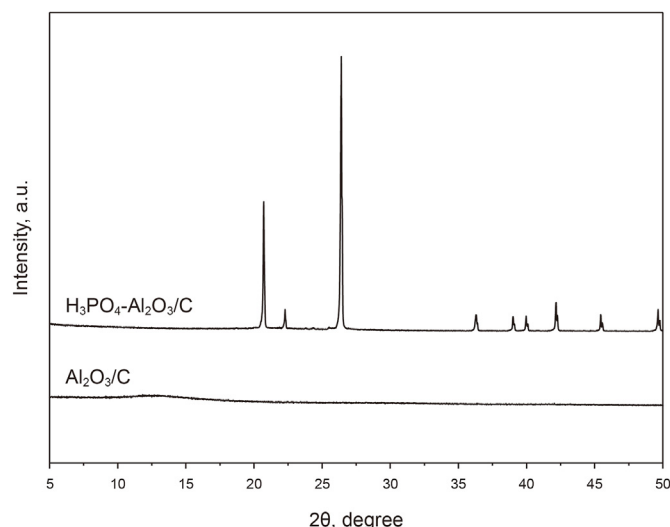

Fig. 2. N$_2$ absorption-desorption isotherms of S-11, CS-11 and ACS-11.

Fig. 4. XRD patterns of Al_2O_3/C and $H_3PO_4-Al_2O_3/C$.

several characteristic peaks at $2\theta = 20-50°$, which is in line with the PDF standard card of $AlPO_4$ (PDF # 71−1041). The above results indicate that Al_2O_3 has an interaction with phosphoric acid, forming the $AlPO_4$ structure in the process of treating Al_2O_3/C with phosphoric acid. Additionally, Fig. S3 displays the HADDF-STEM result of Al_2O_3/C, Al_2O_3 is uniformly doped in carbon material.

SAPO-11 crystals are easy to aggregate with each other due to the absence of mesoporogen in the synthesis of S-11. As a result, SAPO-11 with large crystallites is obtained (Liu et al., 2014). For CS-11, activated carbon as mesoporogen is dispersed between SAPO-11 crystals, which reduces the contact of these crystals. As a consequence, CS-11 has smaller crystallites and more mesopores than S-11 (Yu et al., 2021). However, activated carbon has weak hydrophilicity, leading to the phase separation between SAPO-11 gel and activated carbon, and thus activated carbon plays an inferior role as mesoporogen. During the preparation of hierarchical ACS-11, Al_2O_3 doped in carbon material has an interaction with phosphoric acid, forming $AlPO_4$ structure. Thereby, the phase separation between Al_2O_3/C and SAPO-11 gel is avoided in the synthesis of ACS-11, and Al_2O_3/C effectively prevents the contact between SAPO-11 crystals. As a consequence, SAPO-11 with small crystallites is obtained. Thereby, ACS-11 has smaller crystallites and more mesopores than S-11 and CS-11.

3.3. Py-IR characterization

Fig. 5 displays the Py-IR spectrums of S-11, CS-11 and ACS-11. The bands at 1455 and 1545 cm^{-1} correspondingly represent the Lewis acid centers (LAC) and Brønsted acid centers (BAC), and the band at 1490 cm^{-1} can be ascribed to the cooperative action of LAC and BAC (Wen et al., 2021). All samples show bands at 1545 and 1455 cm^{-1}, indicating that they all have BAC and LAC.

The amount of total B/L acid centers (TB/LAC) and the amount of medium B/L acid centers (MB/LAC) are calculated at 200 and 300 °C individually. The calculation formula is as follows (Fan et al., 2006):

$$C_{B/L} = AS / m\varepsilon \tag{9}$$

where $C_{B/L}$ and A are the amount of LAC or BAC per quality of samples (μmol g^{-1}) and the absorbance (cm^{-1}), respectively; S and m represent the cross-sectional area (cm^2) and the mass (g) of samples, respectively; and ε is the extinction coefficient (cm μmol^{-1}) (Datka, 1981). As shown in Table 2, the amount of TBAC and

Table 2
Acidities of S-11, CS-11 and ACS-11 determined by Py-IR.

Sample	Acidity, μmol/g			
	200 °C		300 °C	
	LAC	BAC	LAC	BAC
S-11	24.8	23.2	15.4	17.2
CS-11	21.1	28.5	13.3	20.0
ACS-11	33.5	42.1	18.9	26.6

the amount of MBAC over the SAPO-11 samples follow the order ACS-11 > CS-11 > S-11. To explain these results, the contents and coordination environment of Si in S-11, CS-11 and ACS-11 are analyzed by XRF and ^{29}Si MAS NMR.

3.4. ^{29}Si MAS NMR characterization

According to the results of XRF (Table S1), S-11, CS-11 and ACS-11 show similar Si contents. Consequently, the acidities of these prepared SAPO-11 samples are mainly related to the coordination environment of Si atoms (Barthomeuf, 1994). The acidity of SAPO molecular sieves is generated by the substitution of the neutral $AlPO_4$ framework by Si atoms. According to the different formats of Si substitution, it can be divided into SM2 and SM3. In the SM2 substitution method, Si(4Al) is formed through the replacement of one Si for one phosphorus. The silicon islands are formed by the replacement of an adjacent aluminum and phosphorus by two Si atoms in the SM3 substitution method, and Si(nAl,4-nSi) ($0 < n < 4$) is formed at the borders of silicon islands (Barthomeuf, 1994). Small silicon islands are conductive to improve the acidity of SAPO-11, thereby enhancing the activity for alkane hydroisomerization (Yang et al., 2017). Fig. 6 presents the ^{29}Si MAS NMR results of S-11, CS-11 and ACS-11. All SAPO-11 samples exhibit five resonance peaks in the range of −80 to −115 ppm. The structures of Si(4Al), Si(3Al,1Si), Si(2Al,2Si), Si(1Al,3Si) and Si(4Si) are centered at −86, −95, −101, −106 and −112 ppm, respectively (Fan et al., 2012).

The proportions of different Si species in SAPO-11 are shown in Table 3. The size of silicon islands decreases following the sequence S-11 > CS-11 > ACS-11. Consequently, the amount of MBAC of ACS-11 is the maximum among these samples, which corresponds to the results of Py-IR. According to the results of Py-IR and ^{29}Si MAS-NMR, the addition of activated carbon or Al_2O_3/C increases the

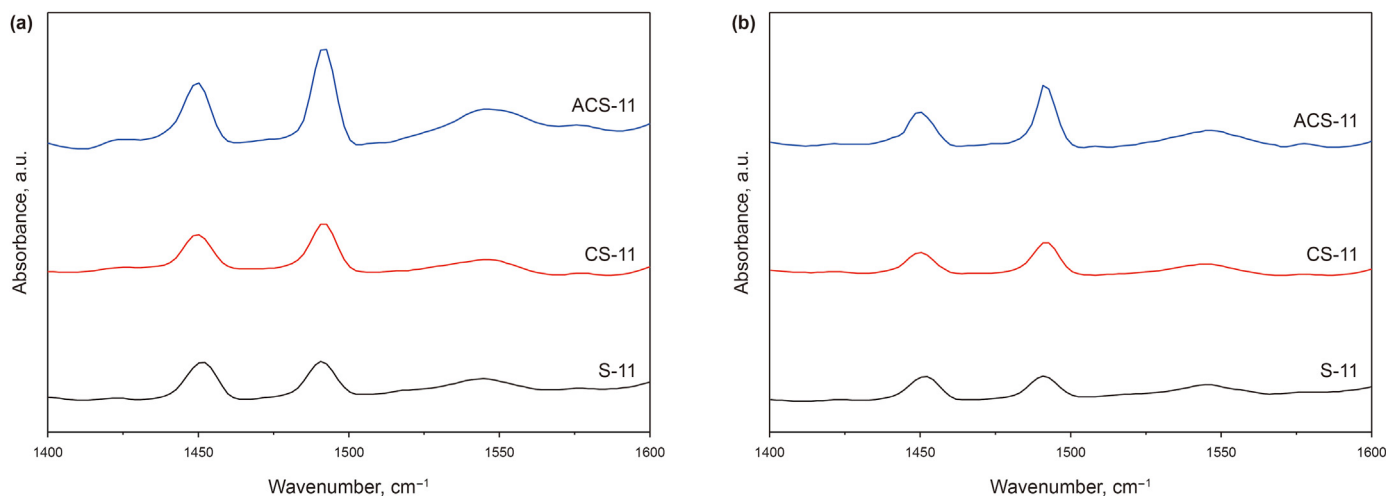**Fig. 5.** Py-IR spectrums of S-11, CS-11 and ACS-11 at 200 (**a**) and 300 °C (**b**).
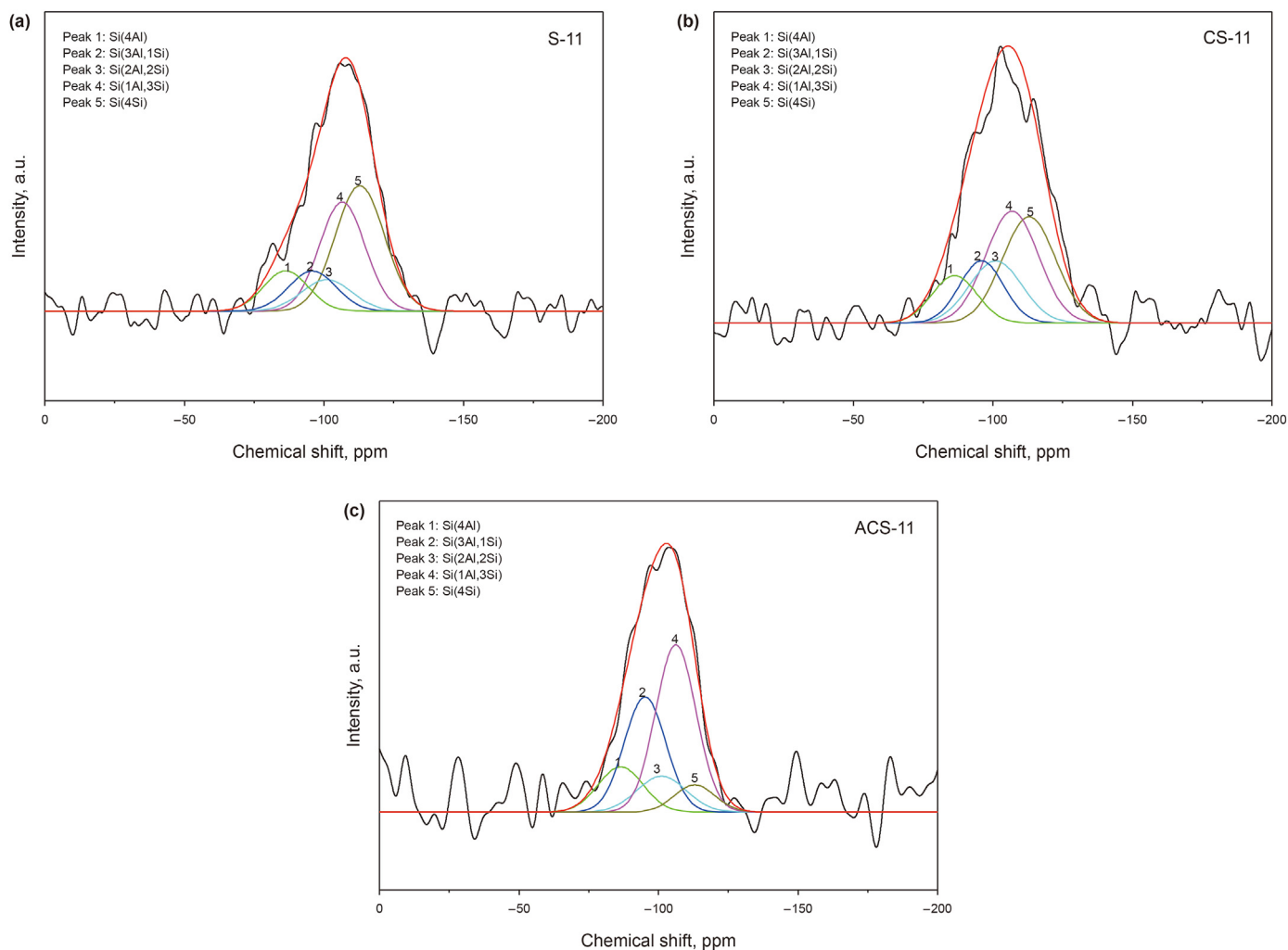
Fig. 6. ^{29}Si MAS NMR spectra of S-11 (**a**), CS-11 (**b**)and ACS-11 (**c**).

Table 3
Proportions of different Si species in S-11, CS-11 and ACS-11.

Sample	Si (4Al), % −86 ppm	Si (3Al, 1Si), % −95 ppm	Si (2Al, 2Si), % −101 ppm	Si (1Al, 3Si), % −106 ppm	Si (4Si), % −112 ppm
S-11	10.9	11.5	9.6	30.3	37.7
CS-11	10.9	13.9	16.6	29.9	28.7
ACS-11	12.3	29.1	10.8	41.1	6.7

amount of MBAC of SAPO-11. This is because Si atoms are promoted to enter the SAPO-11 framework with the existence of activated carbon, which improves Si distribution in the SAPO-11 framework (Yu et al., 2021). As a result, the amount of MBAC of CS-11 is larger than that of S-11. Compared with activated carbon, Al_2O_3/C is better dispersed between SAPO-11 crystals and thus further improves Si distribution in SAPO-11 framework. Consequently, ACS-11 possesses the largest amount of MBAC among these samples.

3.5. Catalytic performance

The n-decane hydroisomerization over Pt/S-11, Pt/CS-11 and Pt/ACS-11 are evaluated, and the evaluation results over these catalysts at 300−360 °C, 2.0 MPa, a weight hourly space velocity (WHSV) of 2.0 h^{-1} and a HDVR of 400 are presented in Fig. S4, which shows that 340 °C is considered as the optimal reaction

temperature for n-decane hydroisomerization over these Pt/SAPO-11 catalysts. Additionally, the n-decane hydroisomerization performances over these catalysts at 340 °C, different WHSVs of 2.0−25 h^{-1}, 2.0 MPa and a HDVR of 400 are displayed in Fig. 7. The n-decane conversion of these catalysts decreases in the wake of the increase of WHSV (Fig. 7(a)). As the n-decane conversion rises, S_T decreases (Fig. 7(b)) and both S_{Mu} and S_C increase for all catalysts (Fig. 7(c) and (d)). The n-decane conversion at the same WHSV follows this order Pt/ACS-11 > Pt/CS-11 > Pt/S-11; S_T and S_{Mu} at the same n-decane conversion decrease in the same sequence, and the S_C increases following the sequence Pt/ACS-11 < Pt/CS-11 < Pt/S-11 in the whole range of n-decane conversion. However, the difference of S_T and S_C over these catalysts is small under the low n-decane conversion, while the gap of them gradually rises with the increasing n-decane conversion. According to the typical bifunctional reaction mechanism of n-alkane hydroisomerization, the n-
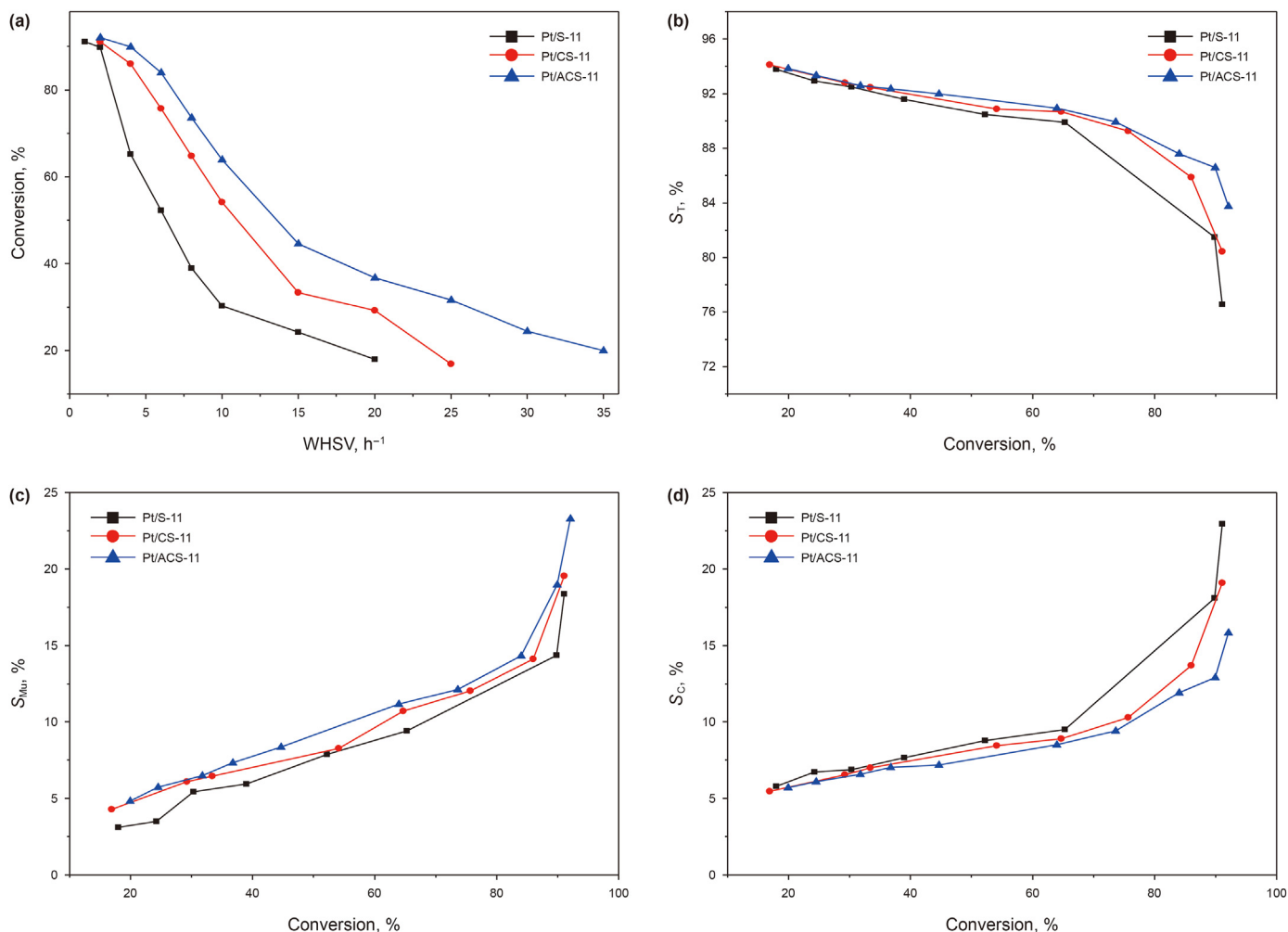
Fig. 7. n-decane conversion versus WHSV (**a**); S_T (**b**), S_{Mu} (**c**) and S_C (**d**) versus conversion for Pt/S-11, Pt/CS-11 and Pt/ACS-11.

decane isomerization process can be expressed as: n-decane → mono-branched C_{10} isomers → multi-branched C_{10} isomers, and the isomerization process is accompanied by cracking reactions (Deldari, 2005). In this work, the low n-decane conversion is due to the high WHSV, which results in the short residence time of reactants at the active sites of catalysts (Singh et al., 2014). As a result, the cracking selectivity is low and the C_{10} isomers selectivity is high over the three catalysts. Therefore, there is a little difference in the S_T and S_C over the three catalysts under the low n-decane conversion (Yang et al., 2019; Wen et al., 2020). However, with the decrease in the WHSV, the n-decane conversion rises, and the difference in the S_T and S_C over the three catalysts gradually increases. ACS-11 has more mesopores, smaller crystallite size and larger ESA than S-11 and CS-11, which promote the formation and diffusion of isomerized intermediates and suppress cracking reactions. Therefore, there is an obvious difference in S_T and S_C between Pt/ACS-11 and the counterparts under the high n-decane conversion.

The n-decane hydroisomerization results over the Pt/SAPO-11 catalysts are shown in Table 4. The primary n-decane hydroisomerization products on Pt/S-11, Pt/CS-11 and Pt/ACS-11 are 2-methylnonane (2-MC9), 3-ethyloctane (3-EC8), 3-methylnonane (3-MC9), 4-ethyloctane (4-EC8), 4-methylnonane (4-MC9), 5-methylnonane (5-MC9), 2,5-dimethyloctane (2,5-DMC8), 3,5-dimethyloctane (3,5-DMC8), 4,5-dimethyloctane (4,5-DMC8), 2,6-

Table 4
Results of n-decane hydroisomerization over different Pt/SAPO-11 catalysts.

	Pt/S-11	Pt/CS-11	Pt/ACS-11
k^a, 10^{-6} mol·g^{-1}·s^{-1}	7.84	10.19	15.25
TOF^a, 10^{-1} s^{-1}	20.43	22.84	25.69
S_T^b, %	76.55	80.45	83.76
S_{Mu}^b, %	18.38	19.53	23.28
S^b, %	—	—	—
2-MC9	8.89	10.04	9.58
3-MC9	15.31	15.00	15.19
4-MC9	6.61	6.44	6.72
5-MC9	22.83	24.79	24.75
3-EC8	2.22	2.38	1.95
4-EC8	2.31	2.27	2.29
2,5-DMC8	2.81	2.49	3.93
2,6-DMC8	5.25	5.19	6.29
2,7-DMC8	3.47	3.06	3.21
3,3-DMC8	0.06	0.10	0.05
3,5-DMC8	0.12	0.18	0.16
3,6-DMC8	4.27	4.64	5.56
4,4-DMC8	1.85	2.16	2.44
4,5-DMC8	0.20	0.26	0.17
3-M-3-EC7	0.19	0.41	0.26
2-M-3-EC7	0.16	0.33	0.23
2-M-5-EC7	—	0.71	0.98
Others, %	0.50	0.46	0.41
S_c^b, %	22.95	19.09	15.83

[a] Obtained at n-decane conversion of 20% and 340 °C.
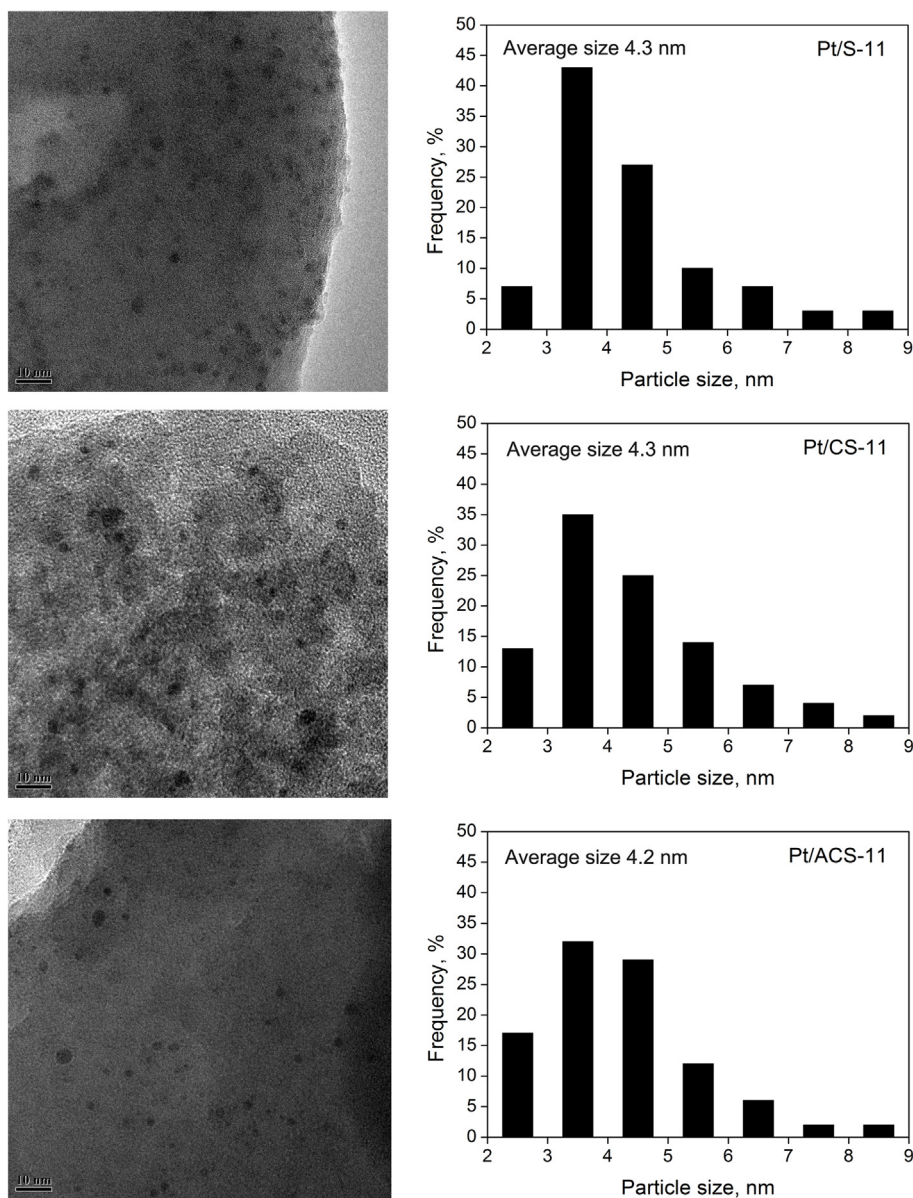[b] Obtained at n-decane conversion of 92% and 340 °C.

Fig. 8. TEM images and size distributions of Pt particles on Pt/S-11, Pt/CS-11 and Pt/ACS-11.

dimethyloctane (2,6-DMC8), 3,6-dimethyloctane (3,6-DMC8), 2,7-dimethyloctane (2,7-DMC8), 4,4-dimethyloctane (4,4-DMC8), 3,3-dimethyloctane (3,3-DMC8), 2-methyl-3-ethylheptane (2-M-3-EC7), 3-methyl-3-ethylheptane (3-M-3-EC7) and 2-methyl-5-ethylheptane (2-M-5-EC7). S_{Mu} of Pt/ACS-11 is 23.28% at the n-decane conversion of approximately 92%, which is higher than those of Pt/S-11 (18.38%) and Pt/CS-11 (19.53%), and S_C of Pt/ACS-11 (15.83%) is lower than those of Pt/S-11 (22.95%) and Pt/CS-11 (19.09%). Additionally, Pt/ACS-11 has a superior stability for n-decane hydroisomerization, which is presented in Fig. S5. The rate constant (k) and turnover frequency (*TOF*) values of Pt/ACS-11 obtained at the n-decane conversion of 20% are 15.25×10^{-6} mol g^{-1} s^{-1} and 25.69×10^{-1} s^{-1} individually, which is higher than those of Pt/S-11 (7.84×10^{-6} mol g^{-1} s^{-1} and 20.43×10^{-1} s^{-1}) and Pt/CS-11(10.19×10^{-6} mol g^{-1} s^{-1} and 22.84×10^{-1} s^{-1}).

The n-decane hydroisomerization over Pt/SAPO-11 catalysts follows a typical bifunctional reaction mechanism (Martens et al., 1986; Deldari, 2005; Zhang et al., 2019), and the details are

displayed in Fig. S6. Firstly, n-decane is dehydrogenated over platinum to produce corresponding n-decene intermediates; then, these intermediates are quickly transferred to the BAC inside the pore of SAPO-11 and occur a skeletal rearrangement reaction to form mono-branched C$_{10}$ intermediates. Based on the theory of "pore mouth/key-lock" (Zhang et al., 2018a; Liu et al., 2020), one side of the mono-branched C$_{10}$ intermediates can be adsorbed on the pore mouth of SAPO-11, and another side is adsorbed on the BAC of the adjacent pore mouth to undergo skeletal isomerization and generate multi-branched C$_{10}$ intermediates. These n-decane branched intermediates can also be cracked on the BAC of SAPO-11. Finally, these branched n-decane intermediates are transferred on the Pt metal sites for hydrogenation to produce C$_{10}$ isomers.

The loadings amount of Pt in these Pt/SAPO-11 catalysts are 0.5 wt%, which meet the hydrogenation-dehydrogenation requirements of alkanes hydroisomerization (Wen et al., 2021). Fig. 8 presents the TEM pictures and Pt particle size distributions of Pt/S-11, Pt/CS-11 and Pt/ACS-11. The average Pt particle size and
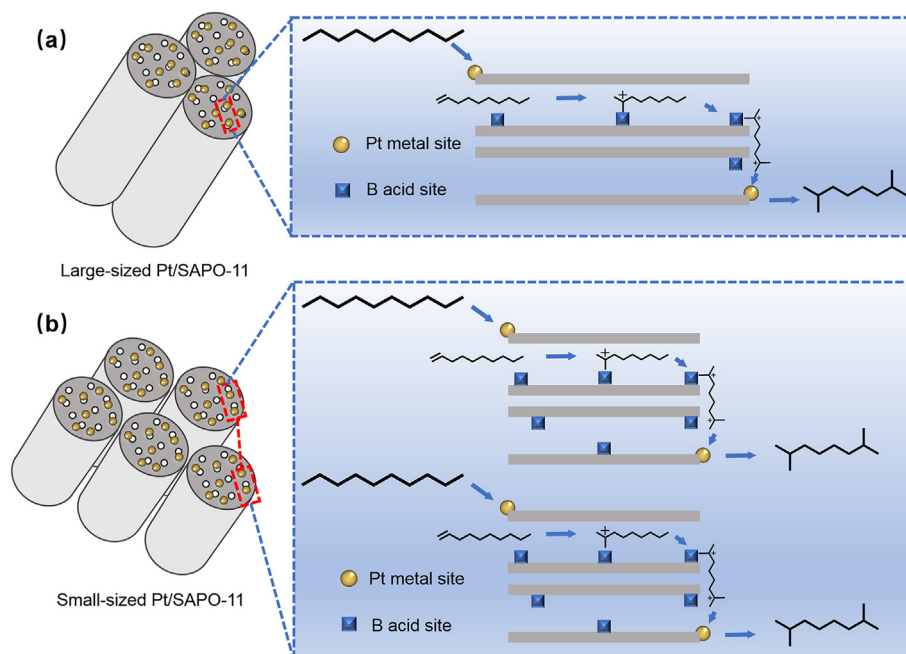
Fig. 9. Schematics of the formation of branched n-decane isomers over Pt/SAPO-11 with different crystallites.

dispersions over Pt/S-11 and Pt/CS-11 are both 4.3 nm and 56%, respectively, and which over Pt/ACS-11 are 4.2 nm and 57% individually. The nearly same particle size and dispersion of Pt suggests that the performance of n-decane hydroisomerization over these catalysts chiefly depends on the physicochemical properties of S-11, CS-11 and ACS-11.

Fig. 9 exhibits the forming schematics of the of branched n-decane isomers over Pt/SAPO-11 with different crystallites. SAPO-11 with a small amount of MBAC and large crystallites offers few active sites and long diffusion path in n-decane hydroisomerization, which is disadvantageous for the generation and diffusion of isomerized intermediates and products (Noh et al., 2018; Oenema et al., 2020). S-11 with less MBAC and larger crystallites than CS-11 and ACS-11 provides a smaller number of hydroisomerization sites and a longer residence time for isomerized intermediates and products over Pt/S-11 than Pt/CS-11 and Pt/ACS-11 (Fig. 9(a)). Consequently, Pt/S-11 presents low S_T and high S_C. Fig. 9(b) shows that SAPO-11 with small crystallites and a large amount of MBAC provides a great amount of hydroisomerization sites and a short diffusion path in n-decane hydroisomerization, which enhances the generation of branched isomers and reduces the cracking side reactions. Pt/ACS-11 presents the maximum n-decane conversion in n-decane hydroisomerization among these catalysts. This can be attributed to the fact that ACS-11 has the largest amount of MBAC among these SAPO-11 samples, which provides a large number of active sites for the n-decane hydroisomerization. Additionally, Pt/ACS-11 shows the maximum S_T and the minimum S_C among these catalysts. This is because ACS-11 has the smallest crystallites and the largest mesopore volume among these samples, which makes the isomerized C_{10} intermediates easy to diffuse out the pores of ACS-11 and thereby reduces the cracking reactions and enhances the production of C_{10} isomers. Furthermore, based on the "pore mouth/key-lock" mechanism, the multi-branched alkane isomers are generated at the ESA rather than in the SAPO-11 channels due to their larger diameters than in the pore openings of SAPO-11 (Claude and Martens, 2000), and a high ESA for SAPO-11 favors the formation of multi-branched C_{10} intermediates. Thus, ACS-11 with higher ESA than S-11 and CS-

11 endows the corresponding catalyst with the maximum S_{Mu} among the three catalysts. Additionally, the maximum Y_T and Y_{Mu} of Pt/ACS-11 are 77.85% and 21.44% individually, which is higher than those of Pt/S-11 (73.21% and 16.75%) and Pt/CS-11(73.85% and 17.19%) (Fig. S7), and also higher than those of the reported catalysts in literatures (Table S2).

4. Conclusions

Hierarchical SAPO-11 molecular sieve was prepared using the Al_2O_3/C composite derived from Al-based metal-organic framework as mesoporogen. The Al_2O_3/C reacts with phosphoric acid to generate the $AlPO_4$/C structure during the synthesis of hierarchical SAPO-11, which efficiently disperses the Al_2O_3/C in the synthesis gel of SAPO-11 and thereby inhibits the aggregation of SAPO-11 crystals. Consequently, the optimal hierarchical SAPO-11 is obtained with smaller crystallites, a bigger mesopore volume (0.13 cm^3 g^{-1}) and a greater amount of MBAC (26.6 μmol g^{-1}) than the conventional SAPO-11 and the hierarchical SAPO-11 employing activated carbon as mesoporogen. Additionally, its corresponding catalyst displays the maximum selectivity to multi-branched C_{10} isomers (23.28%), the minimum cracking selectivity (15.83%) and a superior stability in n-decane hydroisomerization among the prepared catalysts. This work provides a new route for preparing hierarchical silicoaluminophosphate molecular sieve-based catalysts with superior alkane hydroisomerization performances.

Appendix A. Supplementary data

Supplementary data to this article can be found online at https://doi.org/10.1016/j.petsci.2022.06.003.

References

Barrett, E.P., Joyner, L.G., Halenda, P.P., 1951. The determination of pore volume and area distributions in porous substances. I. computations from nitrogen isotherms. J. Am. Chem. Soc. 73 (1), 373–380. https://doi.org/10.1021/ja01145a126.

Barthomeuf, D., 1994. Topological model for the compared acidity of SAPOs and SiAl zeolites. Zeolites. 14 (6), 394–401. https://doi.org/10.1016/0144-2449(94)90164-3.

Bértolo, R., Silva, J.M., Ribeiro, F., et al., 2014. Effects of oxidant acid treatments on carbon-templated hierarchical SAPO-11 materials: synthesis, characterization and catalytic evaluation in n-decane hydroisomerization. Appl. Catal. Gen. 485, 230–237. https://doi.org/10.1016/j.apcata.2014.08.006.

Cartlidge, S., Nissen, H.U., Wessicken, R., 1989. Ternary mesoporous structure of ultrastable zeolite CSZ-1. Zeolites. 9 (4), 346–349. https://doi.org/10.1016/0144-2449(89)90083-3.

Chen, X.X., Vicente, A., Qin, Z.X., et al., 2016. The preparation of hierarchical SAPO-34 crystals via post-synthesis fluoride etching. Chem. Commun. 52, 3512–3515. https://doi.org/10.1039/C5CC09498D.

Chi, K.B., Zhao, Z., Tian, Z.J., et al., 2013. Hydroisomerization performance of platinum supported on ZSM-22/ZSM-23 intergrowth zeolite catalyst. Petrol. Sci. 10 (2), 242–250. https://doi.org/10.1007/S12182-013-0273-6.

Christensen, C.H., Schmidt, I., Carlsson, A., et al., 2005. Crystals in crystalssnanocrystals within mesoporous zeolite single crystals. J. Am. Chem. Soc. 127 (22), 8098–8102. https://doi.org/10.1021/ja050380u.

Claude, M.C., Martens, J.A., 2000. Monomethyl-branching of long n-alkanes in the range from decane to tetracosane on Pt/H-ZSM-22 bifunctional catalyst. J. Catal. 190 (1), 39–48. https://doi.org/10.1006/jcat.1999.2714.

Danilina, N., Krumeich, F., Van Bokhoven, J.A., 2010. Hierarchical SAPO-5 catalysts active in acid-catalyzed reactions. J. Catal. 272 (1), 37–43. https://doi.org/10.1016/j.jcat.2010.03.014.

Datka, J., 1981. Dehydroxylation of NaHY zeolites studied by infrared spectroscopy. J. Chem. Soc., Faraday Trans. 1: Physical Chemistry in Condensed Phases. 77 (12), 2877–2881. https://doi.org/10.1039/F19817702877.

Deldari, H., 2005. Suitable catalysts for hydroisomerization of long-chain normal paraffins. Appl. Catal. Gen. 293, 1–10. https://doi.org/10.1016/j.apcata.2005.07.008.

Deng, S.S., Peng, F.M., 2019. Preparation of MOFs MIL-96 and its adsorption property on naphthalene. N. Chem. Mater. 47 (8), 163–168 (in Chinese).

Eswaramoorthi, I., Lingappan, N., 2003. Hydroisomerization of n-hexane over bimetallic bifunctional silicoaluminophosphate based molecular sieves. Appl. Catal. Gen. 245 (1), 119–135. https://doi.org/10.1016/S0926-860X(02)00637-3.

Fan, Y., Lei, D., Shi, G., et al., 2006. Synthesis of ZSM-5/SAPO-11 composite and its application in FCC gasoline hydro-upgrading catalyst. Catal. Today. 114 (4), 388–396. https://doi.org/10.1016/j.cattod.2006.02.050.

Fan, Y., Xiao, H., Shi, G., et al., 2012. Alkylphosphonic acid- and small aminetemplated synthesis of hierarchical silicoaluminophosphate molecular sieves with high isomerization selectivity to di-branched paraffins. J. Catal. 285 (1), 251–259. https://doi.org/10.1016/j.jcat.2011.09.037.

Groen, J.C., Jansen, J.C., Moulijin, J.A., et al., 2004. Optimal aluminum-assisted mesoporosity development in MFI zeolites by desilication. J. Phys. Chem. B 108 (35), 13062–13065. https://doi.org/10.1021/jp047194f.

Guo, C.M., Wang, W., Zhang, Y., et al., 2021. Influences of the metal-acid proximity of Pd-SAPO-31 bifunctional catalysts for n-hexadecane hydroisomerization. Fuel Process. Technol. 214, 106717–106725. https://doi.org/10.1016/j.fuproc.2020.106717.

Guo, L., Fan, Y., Bao, X.J., et al., 2013. Two-stage surfactant-assisted crystallization for enhancing SAPO-11 acidity to improve n-octane di-branched isomerization. J. Catal. 301, 162–173. https://doi.org/10.1016/j.jcat.2013.02.001.

Harmel, J., Roberts, T., Zhang, Z.R., et al., 2020. Bifunctional molybdenum oxide/acid catalysts for hydroisomerization of n-heptane. J. Catal. 390, 161–169. https://doi.org/10.1016/j.jcat.2020.08.004.

Jacobsen, C.J.H., Madsen, C., Houzvicka, J., et al., 2000. Mesoporous zeolite single crystals. J. Am. Chem. Soc. 122 (29), 7116–7117. https://doi.org/10.1021/ja000744c.

Jaroszewska, K., Fedyna, M., Trawczyński, J., 2019. Hydroisomerization of long-chain n-alkanes over Pt/AlSBA-15+zeolite bimodal catalysts. Appl. Catal. B Environ. 255, 117756–117766. https://doi.org/10.1016/j.apcatb.2019.117756.

Jin, C.L., Ma, B., Zhang, X.W., et al., 2009. Catalytic performance of Pt/HY-β in n-octane hydroisomerization. Petrol. Sci. 6 (3), 299–305. https://doi.org/10.1007/S12182-009-0048-2.

Kang, X., Rao, X.R., Yuan, P., et al., 2021. Al-functionalized mesoporous SBA-15 with enhanced acidity for hydroisomerization of n-octane. Fuel Process. Technol. 215, 106765–106775. https://doi.org/10.1016/j.fuproc.2021.106765.

Kim, J., Kim, W., Seo, Y., et al., 2013. n-Heptane hydroisomerization over Pt/MFI zeolite nanosheets: effects of zeolite crystal thickness and platinum location. J. Catal. 301, 187–197. https://doi.org/10.1016/j.jcat.2013.02.015.

Kim, J., Han, S.W., Kim, J.C., et al., 2018. Supporting nickel to replace platinum on zeolite nanosponges for catalytic hydroisomerization of n-dodecane. ACS Catal. 8 (11), 10545–10554. https://doi.org/10.1021/acscatal.8b03301.

Kimura, T., 2003. Development of Pt/SO$_4^{2-}$/ZrO$_2$ catalyst for isomerization of light naphtha. Catal. Today. 81 (1), 57–63. https://doi.org/10.1016/s0920-5861(03)00102-0.

Lee, H.W., Jeon, J.K., Jeong, K.E., et al., 2013. Hydroisomerization of n-dodecane over Pt/Y zeolites with different acid characteristics. Chem. Eng. J. 232, 111–117. https://doi.org/10.1016/j.cej.2013.07.071.

Li, YM, Liu, ZY, Zhang, QY, et al., 2022. Influence of carbonization temperature on cobalt-based nitrogen-doped carbon nanopolyhedra derived from ZIF-67 for nonoxidative propane dehydrogenation. Petrol. Sci. https://doi.org/10.1016/j.petsci.2022.01.008 (in press).

Lippens, B.C., Boer, J.H.D., 1965. Studies on pore systems in catalysts: V. the t method. J. Catal. 4 (3), 319–323. https://doi.org/10.1016/0021-9517(65)90307-6.

Liu, D.D., Liu, Y.Q., Dai, F.N., et al., 2015. Size- and morphology-controllable synthesis of MIL-96 (Al) by hydrolysis and coordination. Dalton Trans. 44, 16421–16429. https://doi.org/10.1039/C5DT02379C.

Liu, D., Gu, W.Y., Zhou, L., et al., 2022. Recent advances in MOF-derived carbon-based nanomaterials for environmental applications in adsorption and catalytic degradation. Chem. Eng. J. 427, 131503–131521. https://doi.org/10.1016/j.cej.2021.131503.

Liu, S.Y., Ren, J., Zhu, S.J., et al., 2015. Synthesis and characterization of the Fe-substituted ZSM-22 zeolite catalyst with high n-dodecane isomerization performance. J. Catal. 330, 485–496. https://doi.org/10.1016/j.jcat.2015.07.027.

Liu, Y., Qu, W., Chang, W.W., et al., 2014. Catalytically active and hierarchically porous SAPO-11 zeolite synthesized in the presence of polyhexamethylene biguanidine. J. Colloid Interface Sci. 418, 193–199. https://doi.org/10.1016/j.jcis.2013.11.065.

Liu, Y.X., Liu, W.R., Lyu, Y.C., et al., 2020. Intra-crystalline mesoporous SAPO-11 prepared by a grinding synthesis method as FCC promoters to increase iso-paraffin of gasoline. Microporous Mesoporous Mater. 305, 110320–110327. https://doi.org/10.1016/j.micromeso.2020.110320.

López, C.M., Machado, F.J., Goldwasser, J., et al., 1997. The successive crystallization and characterization of sapo-31 and sapo-11 from the same synthesis gel: influence on the selectivity for 1-butene isomerization. Zeolites. 19 (2–3), 133–141. https://doi.org/10.1016/S0144-2449(97)00058-4.

Lv, G., Wang, C.X., Chi, K.B., et al., 2018. Effects of Pt site distributions on the catalytic performance of Pt/SAPO-11 for n-dodecane hydroisomerization. Catal. Today. 316, 43–50. https://doi.org/10.1016/j.cattod.2018.04.072.

Machoke, A.G., Beltrán, A.M., Inayat, A., et al., 2015. Micro/macroporous system: MFI-type zeolite crystals with embedded macropores. Adv. Mater. 27 (6), 1066–1070. https://doi.org/10.1002/adma.201404493.

Martens, J.A., Jacobs, P.A., Weitkamp, J., 1986. Attempts to raltionalize the distribution of hydrocracked products. I qualitative description of the primary hydrocracking modes of long chain paraffins in open zeolites. Appl. Catal. Gen. 20 (1), 239–281. https://doi.org/10.1016/0166-9834(86)80020-3.

Nandan, D., Saxena, S.K., Viswanadham, N., 2014. Synthesis of hierarchical ZSM-5 using glucose as a templating precursor. J. Mater. Chem. 2, 1054–1059. https://doi.org/10.1039/c3ta13904b.

Noh, G., Shi, Z.C., Zones, S.I., et al., 2018. Isomerization and β-scission reactions of alkanes on bifunctional metal-acid catalysts: consequences of confinement and diffusional constraints on reactivity and selectivity. J. Catal. 368, 389–410. https://doi.org/10.1016/j.jcat.2018.03.033.

Oenema, J., Harmel, J., Velez, R.P., et al., 2020. Influence of nanoscale intimacy and zeolite micropore size on the performance of bifunctional catalysts for n-heptane hydroisomerization. ACS Catal. 10 (23), 14245–14257. https://doi.org/10.1021/acscatal.0c03138.

Phienluphon, R., Pinkaew, K., Yang, G.H., et al., 2015. Designing core (Cu/ZnO/Al$_2$O$_3$)–shell (SAPO-11) zeolite capsule catalyst with a facile physical way for dimethyl ether direct synthesis from syngas. Chem. Eng. J. 270, 605–611. https://doi.org/10.1016/j.cej.2015.02.071.

Qin, B., Zhang, X.W., Zhang, Z.Z., et al., 2011. Synthesis, characterization and catalytic properties of Y-β zeolite composites. Petrol. Sci. 8 (2), 224–228. https://doi.org/10.1007/s12182-011-0139-8.

Ren, X., Komarneni, S., Roy, D.M., 1991. The role of gel chemistry in synthesis of aluminophosphate molecular sieves. Zeolites. 11 (2), 142–148. https://doi.org/10.1016/0144-2449(91)80408-R.

Samad, J.E., Blanchard, J., Sayag, C., et al., 2016. The controlled synthesis of metal-acid bifunctional catalysts: the effect of metal: acid ratio and metal-acid proximity in Pt silica-alumina catalysts for n-heptane isomerization. J. Catal. 342, 203–212. https://doi.org/10.1016/j.jcat.2016.08.004.

Sazama, P., Pastvova, J., Kaucky, D., et al., 2018. Does hierarchical structure affect the shape selectivity of zeolites? Example of transformation of n-hexane in hydroisomerization. J. Catal. 364, 262–270. https://doi.org/10.1016/j.jcat.2018.05.010.

Sánchez-Contador, M., Ateka, A., Aguayo, A.T., et al., 2018. Behavior of SAPO-11 as acid function in the direct synthesis of dimethyl ether from syngas and CO$_2$. J. Ind. Eng. Chem. 63, 245–254. https://doi.org/10.1016/j.jiec.2018.02.022.

Singh, A.K., Kondamudi, K., Yadav, R., et al., 2014. Uniform mesoporous silicoaluminophosphate derived by vapor phase treatment: its catalytic and kinetic studies in hydroisomerization of 1-octene. J. Phys. Chem. C 118 (48), 27961–27972. https://doi.org/10.1021/jp509421j.

Vedachalam, S., Boahene, P., Dalai, A.K., 2021. Production of jet fuel by hydrorefining of Fischer-Tropsch wax over Pt/Al-TUD-1 bifunctional catalyst. Fuel. 300, 121008–121118. https://doi.org/10.1016/j.fuel.2021.121008.

Wen, C.L., Han, S.L., Xu, J.D., et al., 2017. A novel route to synthesize SAPO-11 molecular sieves with a high external surface area in the presence of ethylene glycol and supercritical carbon dioxide for 1-octene hydroisomerization to dimethylhexanes. J. Catal. 356, 100–110. https://doi.org/10.1016/j.jcat.2017.05.021.

Wen, C.L., Xu, J.D., Wang, X.M., et al., 2020. n-Heptane hydroisomerization over a SO$_4^{2-}$/ZrO$_2$@SAPO-11 composite-based catalyst derived from the growth of UiO-66 on SAPO-11. Energy Fuels. 34 (8), 9498–9508. https://doi.org/10.1021/

acs.energyfuels.0c01634.

Wen, C.L., Xu, J.D., Wang, X.M., et al., 2021. n-Nonane hydroisomerization over hierarchical SAPO-11-based catalysts with sodium dodecylbenzene sulfonate as a dispersant. Petrol. Sci. 18, 654–666. https://doi.org/10.1007/s12182-021-00544-3.

Xi, D., Sun, Q., Xu, J., et al., 2014. In situ growth-etching approach to the preparation of hierarchically macroporous zeolites with high MTO catalytic activity and selectivity. J. Mater. Chem. 2, 17994–18004. https://doi.org/10.1039/c4ta03030c.

Yang, H., Jia, L., Zhang, Z.P., et al., 2022. Novel cerium-based MOFs photocatalyst for photocarrier collaborative performance under visible light. J. Catal. 405, 74–83. https://doi.org/10.1016/j.jcat.2021.11.017.

Yang, L.M., Xing, S.Y., Sun, H.Z., et al., 2019. Citric-acid-induced mesoporous SAPO-11 loaded with highly dispersed nickel for enhanced hydroisomerization of oleic acid to iso-alkanes. Fuel Process. Technol. 187, 52–62. https://doi.org/10.1016/j.fuproc.2019.01.008.

Yang, Z.C., Li, J.L., Liu, Y.Q., et al., 2017. Effect of silicon precursor on silicon incorporation in SAPO-11 and their catalytic performance for hydroisomerization of n-octane on Pt-based catalysts. J. Energy Chem. 26 (4), 688–694. https://doi.org/10.1016/j.jechem.2017.02.002.

Yang, Z.C., Liu, Y.Q., Li, Y.P., et al., 2019. Effect of preparation method on the bimetallic NiCu/SAPO-11 catalysts for the hydroisomerization of n-octane. J. Energy Chem. 28, 23–30. https://doi.org/10.1016/j.jechem.2017.10.003.

Yao, Y., Tian, Y.J., Wu, H.H., et al., 2015. Pt-promoted and Hβ zeolite-supported Ni₂P catalysts for hydroisomerisation of n-heptane. Fuel Process. Technol. 133, 146–151. https://doi.org/10.1016/j.fuproc.2015.01.033.

Yu, G., Chen, X.Q., Xue, W.J., et al., 2020. Melting-assisted solvent-free synthesis of SAPO-11 for improving the hydroisomerization performance of n-dodecane.

Chin. J. Catal. 41 (4), 622–630. https://doi.org/10.1016/S1872-2067(19)63466-2.

Yu, G., Qiu, M.H., Wang, T., et al., 2021. Optimization of the pore structure and acidity of SAPO-11 for highly efficient hydroisomerization on the long-chain alkane. Microporous Mesoporous Mater. 320, 111076–111085. https://doi.org/10.1016/j.micromeso.2021.111076.

Zhang, P., Liu, H.Y., Yue, Y.Y., et al., 2018a. Direct synthesis of hierarchical SAPO-11 molecular sieve with enhanced hydroisomerization performance. Fuel Process. Technol. 179, 72–85. https://doi.org/10.1016/j.fuproc.2018.06.012.

Zhang, P., Liu, H.Y., Zhu, H.B., et al., 2018b. Synthesis and catalytic application of alumina@SAPO-11 composite via the in situ assembly of silicoaluminophosphate nanoclusters at an alumina substrate. Catal. Sci. Technol. 8, 4209–4218. https://doi.org/10.1039/c8cy00537k.

Zhang, Y.D., Liu, D., Men, Z.W., et al., 2019. Hydroisomerization of n-dodecane over bi-porous Pt-containing bifunctional catalysts: effects of alkene intermediates' journey distances within the zeolite micropores. Fuel 236, 428–436. https://doi.org/10.1016/j.fuel.2018.09.017.

Zhang, Y.P., Xu, J.X., Zhou, J., et al., 2022. Metal-organic framework-derived multifunctional photocatalysts. Chin. J. Catal. 43 (4), 971–1000. https://doi.org/10.1016/S1872-2067(21)63934-7.

Zhao, S.F., Wang, W.D., Wang, L.Z., et al., 2019. Tuning hierarchical ZSM-5 zeolite for both gas- and liquid-phase biorefining. ACS Catal. 10 (2), 1185–1194. https://doi.org/10.1021/acscatal.9b04104.

Zhao, X.L., Liu, W., Wang, J.Q., et al., 2020. Interface mediated crystallization of plate-like SAPO-41 crystals to promote catalytic hydroisomerization. Appl. Catal. Gen. 602, 117738–117750. https://doi.org/10.1016/j.apcata.2020.117738.